Digital Object Identifier 10.1109/TPEL.2020.3006334

IEEE Transactions on Power Electronics

Extended Operation Range of Photovoltaic Inverters by Current Waveform Shaping

Sebastian Brüske
Giovanni De Carne
Giampaolo Buticchi
Marco Liserre
He Zhang

Suggested Citation

S. Brüske, G. De Carne, G. Buticchi, M. Liserre and H. Zhang, "Extended Operation Range of Photovoltaic Inverters by Current Waveform Shaping," in *IEEE Transactions on Power Electronics*, vol. 36, no. 2, pp. 1693-1707, Feb. 2021.

Extended Operation Range of Photovoltaic Inverters by Current Waveform Shaping

Sebastian Brüske, *Student Member, IEEE,* Giovanni De Carne, *Member, IEEE,*
Giampaolo Buticchi, *Senior Member, IEEE,* Marco Liserre, *Fellow, IEEE,* and He Zhang, *Senior Member, IEEE*

***Abstract*—The grid connection of photovoltaic voltage source inverters depends on the dc-link voltage level that can be supplied by the maximum power tracking of the photovoltaic system. The inverter disconnects from the grid, if the minimum required dc-link voltage level is violated, which leads to unwanted energy curtailments implying losses to the system owner. This paper proposes to apply current waveform shaping to the inverter current in order to reduce the peak value of the voltage waveform at the point of common coupling by which the minimum required dc-link voltage level for power injection is reduced. This extended operation range of photovoltaic inverters is achieved through third harmonic current injection and can be applied to single-phase and three-phase, four-wire inverters without additional converter stages. A control structure for harmonic current injection and harmonic phase determination is presented and validated by simulations and the analysis is verified by experiments.**

***Index Terms*—Photovoltaic inverter, harmonic injection, current waveform shaping, distributed generation.**

I. Introduction

THE relevance of photovoltaic (PV) energy sources for power generation is increasing together with the installation of distributed PV generation and large-scale PV power plants. Large PV systems are typically installed in rural areas with optimal irradiance conditions, which are often characterized by weak grid conditions [1], [2] and largely resistive grid. As a consequence, relatively high voltage levels at the point of common coupling (PCC) can occur.

Grid-connected PV voltage source inverters require a minimum dc-link voltage level that is related to the ac voltage peak value in order to avoid over-modulation. Rainy, cloudy days and sunset are examples of situations in which the output capability of PV cells is weakened and in which the system utilization rate decreases as a result of power curtailment and grid disconnection of the PV inverter [3]. PV arrays supply the dc-link voltage either directly or through an additional dc/dc converter stage for an extended dc voltage operation range [4]. Maximum power point tracking (MPPT) algorithms ensure maximum PV power depending on irradiance, shading, temperature and aging conditions [5]. MPPT algorithms are usually implemented in single-stage inverters by controlling its dc voltage [6], [7]. For example, at partial shading, the global maximum can be located below the minimum dc-link voltage. In order to stay within the voltage operation range, the PV array output power reduces or the inverter disconnects from the grid. Grid-side transformers extend the operational area, but they lead to increased costs and weight, as well as to reduced system efficiency [8]. An additional dc/dc converter stage greatly extends the dc voltage operation range, but it increases complexity, volume and costs due to nominal power rating and increased number of components. Various inverter solutions have been proposed in literature to boost the dc voltage with less components or reduced volume [8]–[10]. For example, a mini-boost converter stage with reduced power rating is presented in [8], which is bypassed in normal operation. Depending on specifications, connected to the local annual irradiance and shading conditions, single-stage inverter solutions can be chosen due to lower costs and higher reliability.

The absence of a neutral conductor in three-phase, three-wire systems offers the freedom to shape the modulation signal by adding a zero sequence component in continuous and discontinuous modulation. The goal is to optimize the system performance such as switching loss reduction, power quality improvement, extension of modulation range, and common mode suppression in motor drive applications [11]. In presence of a neutral connection as is the case in single-phase and three-phase, four-wire systems, zero sequence components change the inverter output voltage. An optimization approach for single-phase systems is presented in [12], where both inverter and overall grid efficiency as well as dc-link voltage behavior can be improved by voltage and current waveform shaping through harmonic current injection in single-phase islanded grids, not limited to zero sequence harmonics. Similar approaches are based on 3rd harmonic injection in transmission systems. While [13] presents a power flow controller with distributed dc-link that offers redundancy and lower inverter ratings, [14] proposes to lower the conductor-to-ground clearance and the cost of transmission lines.

This paper proposes to use current waveform shaping (CWFS) in grid connected PV applications connected by 3rd harmonic injection in order to reduce the peak value of the PCC voltage waveform and, consequently, the minimum dc-link voltage level of PV inverters, keeping the fundamen-

Manuscript received July 15, 2019; revised 21 October, 2019, January 22, 2020, April 16, 2020; accepted June 15, 2020. This work was supported by the German Federal Ministry for Economic Affairs and Energy(BMWi) within Project KielFlex "Kiel als Vorbild für die Errichtung von Ladeinfrastruktur in einem flexiblen Stromnetz zur Umsetzung einer Emissionsreduktion im Transportsektor" (01MZ18002D).

S. Brüske and M. Liserre are with the Chair of Power Electronics, Kiel University, 24143 Kiel, Germany (e-mail: {seb, ml}@tf.uni-kiel.de).

G. De Carne is with the Institute for Technical Physics, Karlsruhe Institute ofTechnology, 76131 Karlsruhe, Germany (e-mail: giovanni.carne@kit.edu).

G. Buticchi and H. Zhang are with the Faculty of Science and Engineering, University of Nottingham Ningbo China, Ningbo 315100, China (e-mail: {giampaolo.buticchi, he.zhang}@nottingham.edu.cn).

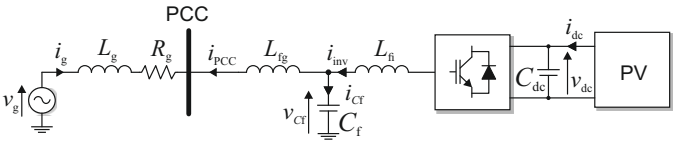

Fig. 1. Grid model based on Thévenin equivalent with restive-inductive impedance and grid-connected PV system with single-stage inverter.

tal voltage component intact. While the method is inactive in normal operations, the 3rd harmonic current injection is enabled in case of minimum dc-link voltage violations. The approach offers an extended voltage operation range without additional conversion stages and is applicable to single-phase and three-phase, four-wire systems by adapting the control and protection algorithms. The IEEE grid standard [15] defines the maximum achievable extension of the voltage operation range by limiting the 3rd harmonic current to 4 % of the rated fundamental current. Therefore, the allowed harmonic current becomes significant in light power conditions and can be used to extend the operation range of PV inverters.

This paper is organized as follows. The voltage operation range of PV systems and the peak voltage reduction as well as its effects on the minimum dc-link voltage and on the rms current are described in Section II. The current control scheme for harmonic current injection and reference calculation is presented in Section III. Furthermore, a harmonic phase determination based on on-line grid estimation is proposed and simulations validate the control concept. Experimental results verify the effectiveness of the proposed approach in Section IV. Conclusions are finally drawn in Section V.

II. Current Waveform Shaping of Photovoltaic Inverters

A typical grid-connected PV system is shown in Fig. 1, which consists of PV array, dc-link and single-stage grid inverter with LCL-filter. The grid is modeled as a Thévenin equivalent with restive-inductive impedance Z_g and grid voltage v_g [16]. In the following, the principle of CWFS is described and existing harmonic injection approaches are discussed. Then, the voltage operation range of PV systems, the peak voltage reduction at the PCC and its impact on the dc-link voltage and inverter current are described. An example illustrates the advantage of the proposed approach in regard of PV output energy and shows its limitations. Furthermore, the harmonic injection level is discussed at the end of this section.

A. Current Waveform Shaping and Harmonic Injection

The basic principle of waveform shaping is described in [12] with the aim to increase the fundamental voltage component for reduced current level operations. In this work, the objective of waveform shaping is similar to the approach proposed in [14]. The peak value of the sinusoidal voltage is reduced by 3rd harmonic current injection, while the fundamental voltage component remains intact. The reduced ac voltage level implies a reduced minimum dc-link voltage at inverter side, which offers an extended voltage operation range.

The objectives of the harmonic injection approaches [12]–[14] are different, but a common principle is the utilization of harmonic frequencies for optimization, which also leads to a common challenge: the harmonic impact. The concept of [12] to increase the overall system efficiency is limited to small-scale, isolated systems with components that can operate in conditions with high harmonic content, mostly fulfilled by components with power electronics interfaces. Protection operation needs to be tested in such conditions. Distributing the functionality of a single unified power flow controller to a shunt inverter and several smaller rated, single-phase series inverters by connecting the distributed dc-links through the 3rd harmonic, as proposed in [13], prevents from system shutdown in case of series inverter failure and offers lower inverter costs. However, harmonic losses have to be considered in the transmission line and delta-star transformers that are required to step down the voltage level and to isolate the harmonic frequency. Furthermore, protection has to operate as specified. The same challenges arise in [14], where the phase voltages of a transmission line are lowered by 3rd harmonic current injection, keeping the line-to-line voltages intact, by which the ground clearance of transmission towers can be reduced. If instead the fundamental voltage component is increased, the line loadability can be increased. However, the line-to-line voltages change in the latter objective, leading to an increased voltage level. Additional challenge is the length of transmission lines. With increasing line length, the effect of traveling electromagnetic waves provoke a phase displacement between fundamental and 3rd harmonic voltages, which counteracts the phase voltage reduction and which needs to be compensated. Furthermore, the Ferranti effect that sets limits to the length of ac transmission lines, should be taken into consideration for the harmonic frequency.

In contrast to these harmonic injection approaches, the constraint of harmonic injection of the proposed method for PV applications is to stay in compliance with grid standards [15]. This means that the associated harmonic impact is already included in the design of the actual grid and its components such as protection.

B. Extended Operation of Photovoltaic Inverters

The operation of a single-stage PV inverter is depicted in Fig. 2(a) mainly divided into a nominal power operation area and two areas, which are non-operational due to voltages below the minimum required dc-link voltage $V_\mathrm{dc,min}$ and due to voltages above the maximum $V_\mathrm{dc,max}$. Above the maximum voltage, the inverter operates in power limitation until an overvoltage threshold is reached, from which on the inverter is non-operational. In the nominal power area, the inverter can operate at nominal power $P_\mathrm{dc,N}$ as long as $V_\mathrm{dc,min}\,(I_\mathrm{N})$ is not violated, which depends on the nominal current of the PV system. Below this voltage, it can operate in power limitation depending on $V^{(1)}_\mathrm{dc,min}$, which is a function of the actual PV grid-side current i_PCC. The described behavior results in the peak power envelope shown in Fig. 2.

Two-stage inverter solutions or the mini-boost solution proposed in [8] extend the operational area by boosting lower

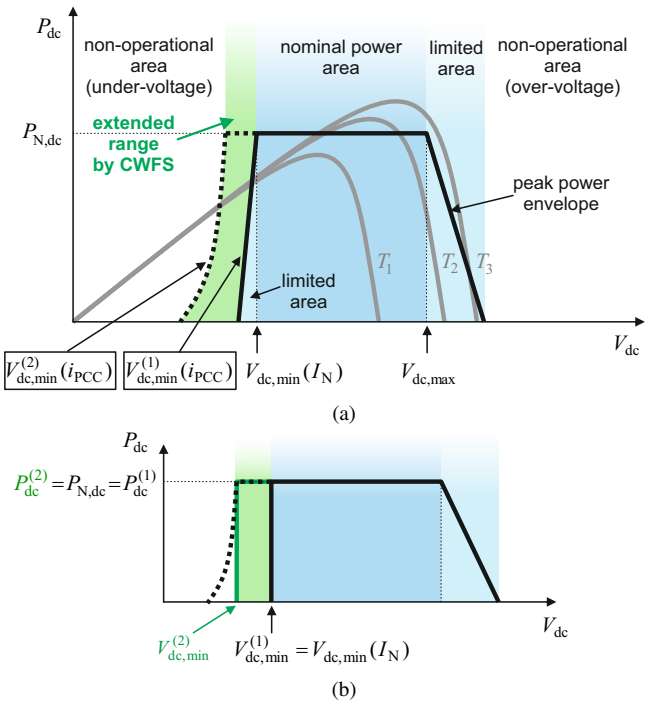

Fig. 2. Voltage operation range of single-stage PV inverters: (a) CFWS operation extension, (b) Protection concept based on nominal power injection.

voltages. This work instead proposes to shift the minimum dc-link voltage from $V^{(1)}_{\mathrm{dc,min}}$ to $V^{(2)}_{\mathrm{dc,min}}$ by decreasing the PCC peak voltage value through 3rd harmonic current injection. The elevated (1) in $V^{(1)}_{\mathrm{dc,min}}$ denotes the situation without CWFS and elevated (2) the same conditions with CWFS. Additional stages or other components are not required, and the concept is applicable in single-phase or three-phase, four-wire inverters by adapting control and protection algorithms. An example of a protection concept is shown in Fig. 2(b) based on nominal power injection. In normal operation without CWFS, the inverter would disconnect if the voltage falls below $V^{(1)}_{\mathrm{dc,min}}$, which is in this example the minimum dc-link voltage required for nominal power injection. The operation range can be extended by CWFS implementation, shifting the minimum dc-link voltage from $V^{(1)}_{\mathrm{dc,min}}$ to $V^{(2)}_{\mathrm{dc,min}}$, which is the minimum dc-link voltage required for nominal power injection at CWFS operation. A possible protection algorithm to implement this concept is presented in Section IV. The area between dotted line and green area is an unused potential in this example, since the level depends on nominal power injection. By varying $P^{(2)}_{\mathrm{dc}}$ optimization problems can be formulated for the trade-off between minimum dc-link voltage reduction and power level.

C. Peak Voltage Reduction at PCC

The effect of 3rd harmonic injection on the PCC voltage depends on the grid impedance Z_{g} and the short circuit capacity (SCC), which is a measure of the power flowing in a specific point in the grid in case of a short circuit. The SCC is a function of the rated grid voltage V_{g} and Z_{g}. Two indicators, the short circuit ratio (SCR) and the X/R-ratio $r_{X/R}$, are used to describe the grid behavior. If a PV system with nominal power $S_{\mathrm{N,PV}}$ is connected to a specific point in the grid, the SCR follows from

$$\mathrm{SCR} = \frac{\mathrm{SCC}}{S_{\mathrm{N,PV}}} = \frac{V_{\mathrm{g}}^2}{Z_{\mathrm{g}} \cdot S_{\mathrm{N,PV}}} \,. \tag{1}$$

Weak grids are characterized by SCR below 10. The resistive part R_{g} and the inductive part X_{g} of the grid impedance are calculated by

$$X_{\mathrm{g}} = \frac{Z_{\mathrm{g}}}{\sqrt{1+\left(\frac{1}{r^2_{X/R}}\right)}} \qquad R_{\mathrm{g}} = \frac{Z_{\mathrm{g}}}{\sqrt{1+r^2_{X/R}}} \,. \tag{2}$$

The idea of peak voltage reduction at the PCC by 3rd harmonic injection is illustrated in Fig. 3 showing the phasor diagram of the fundamental system in Fig. 3(a) and of the 3rd harmonic system in Fig. 3(b). The superposition of both frequency systems is depicted in Fig. 3(c) focusing on the PCC voltages and currents. While the fundamental voltage and current components rotate at base frequency ω_0, the 3rd harmonic components are rotating at $3\omega_0$ around their respective fundamental component. With the right set of parameters, the 3rd harmonic voltage at the PCC is at its minimum, when the fundamental voltage component reaches its maximum, which cuts the peak of the voltage waveform leading to a reduced voltage level. A reduced voltage level at the PCC decreases the inverter voltage, which is required for grid operations. In order to analyze the potential for voltage reduction at the PCC and for reduction of the minimum dc-link voltage level, the phase of the 3rd harmonic current needs to be calculated. For optimal voltage reduction, the fundamental and 3rd harmonic voltages at the PCC are required to be in phase to each other. In the following analysis, a three-phase, four-wire system is considered. The first step to analyze the influence on the PCC voltage is to calculate V_{PCC} at fundamental frequency without harmonic injection in relationship to the power injected by the PV system. Considering $\underline{V}_{1,\mathrm{PCC}}$ as the reference voltage for phasor calculations, the complex power follows from

$$\begin{aligned} \underline{S}_{1,\mathrm{PCC}} &= P_1 + jQ_1 = 3 \cdot V_{1,\mathrm{PCC}} \cdot \underline{I}^*_{1,\mathrm{PCC}} \\ &= 3 \cdot V_{1,\mathrm{PCC}} \cdot \left(\frac{V_{1,\mathrm{PCC}} - \underline{V}_{1,\mathrm{g}}}{R_{\mathrm{g}} + jX_{1,\mathrm{g}}} \right)^* \,. \end{aligned} \tag{3}$$

Then, $V_{1,\mathrm{PCC}}$ can be derived from (3) with the complex voltages and currents written as

$$\begin{aligned} \underline{V} &= V \cdot (\cos(\theta) + j \cdot \sin(\theta)) \\ \underline{I} &= V \cdot (\cos(\varphi) + j \cdot \sin(\varphi)) \end{aligned} \tag{4}$$

$$\begin{aligned} \left(V^2_{1,\mathrm{PCC}}\right)^2 - V^2_{1,\mathrm{PCC}} \cdot \left(V^2_{1,\mathrm{g}} + 2R_{\mathrm{g}} \frac{P_1}{3} + 2X_{1,\mathrm{g}} \frac{Q_1}{3} \right) \\ + \left(\left(\frac{P_1}{3}\right)^2 + \left(\frac{Q_1}{3}\right)^2 \right) \cdot \left(R^2_{\mathrm{g}} + X^2_{1,\mathrm{g}}\right) = 0 \,. \end{aligned} \tag{5}$$

Only one solution of (5) leads to a possible grid situation, from which the PCC current can be calculated:

$$I_{1,\mathrm{PCC}} = \frac{S_{1,\mathrm{PCC}}}{3 \cdot V_{1,\mathrm{PCC}}} \,. \tag{6}$$

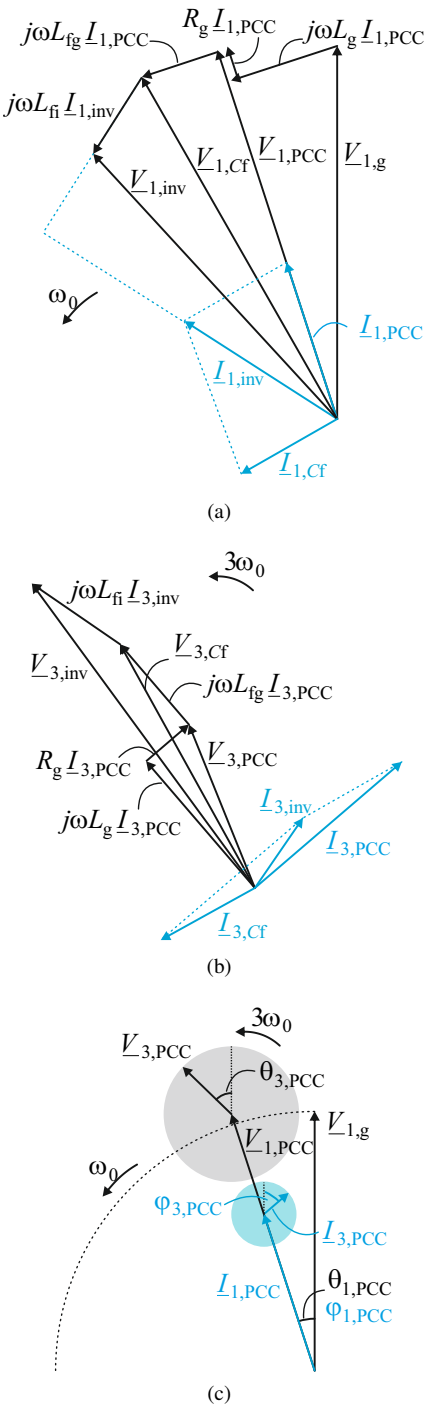

Fig. 3. Phasor diagrams: (a) Fundamental frequency system, (b) 3rd harmonic system, (c) superposition of the fundamental and 3rd harmonic frequency systems at PCC.

As second step, (7) can be set up from Fig. 1 based on Kirchhoff's law, now using $\underline{V}_{\mathrm{g}}$ as reference voltage for phasor calculations:

$$\underline{V}_{1,\mathrm{PCC}} = V_{1,\mathrm{g}} + R_{\mathrm{g}} \cdot \underline{I}_{1,\mathrm{PCC}} + jX_{1,\mathrm{g}} \cdot \underline{I}_{1,\mathrm{PCC}} \,. \tag{7}$$

Using (4) and with

$$\varphi_{1,\mathrm{x}} = \theta_{1,\mathrm{PCC}} - \varphi_{1,\mathrm{PCC}} \tag{8}$$

as the power angle at the PCC, the phase of $\underline{I}_{1,\mathrm{PCC}}$ can be derived

$$\varphi_{1,\mathrm{PCC}} = -\varphi_{1,\mathrm{x}} - \sin^{-1}\left(\frac{I_{1,\mathrm{PCC}} \cdot (R_{\mathrm{g}} \cdot \sin\varphi_{1,\mathrm{x}} - X_{1,\mathrm{g}} \cdot \cos\varphi_{1,\mathrm{x}})}{V_{1,\mathrm{g}}}\right) . \tag{9}$$

Hence, $\underline{V}_{1,\mathrm{PCC}}$ follows from (7) using (6) and (9). The third step is the calculation of the 3rd harmonic current, which needs to be injected by the PV inverter in order to obtain the desired voltage waveform. The 3rd harmonic current level follows from

$$I_{3,\mathrm{PCC}} = r_{i,3} I_{\mathrm{N,PCC}} \,, \tag{10}$$

where $I_{\mathrm{N,PCC}}$ is the nominal current of the PV system and $r_{i,3}$ the maximum harmonic ratio allowed by grid standards [15] for single harmonic frequencies in the low-frequency range. The phase $\varphi_{3,\mathrm{PCC}}$ depends on the PCC voltage of the fundamental frequency. It is required that the resulting 3rd harmonic voltage component $\underline{V}_{3,\mathrm{PCC}}$ is in phase to $\underline{V}_{1,\mathrm{PCC}}$:

$$\theta_{3,\mathrm{PCC}} = 3 \cdot \theta_{1,\mathrm{PCC}} \,. \tag{11}$$

Under the assumption that the 3rd harmonic is not present in the grid ($\underline{V}_{3,\mathrm{g}} = 0$), Eq. (7) can be written for the 3rd harmonic system:

$$\underline{V}_{3,\mathrm{PCC}} = R_{\mathrm{g}} \cdot \underline{I}_{3,\mathrm{PCC}} + jX_{3,\mathrm{g}} \cdot \underline{I}_{3,\mathrm{PCC}} \,. \tag{12}$$

The phase of $\underline{I}_{3,\mathrm{PCC}}$ is derived from (12)

$$\varphi_{3,\mathrm{PCC}} = \tan^{-1}\left(-\frac{jX_{3,\mathrm{g}}}{R_{\mathrm{g}}}\right) + \theta_{3,\mathrm{PCC}} \tag{13}$$

and finally, $\underline{V}_{3,\mathrm{PCC}}$ follows from (12). The combination of both fundamental and 3rd harmonic system gives the resulting waveform $v_{\mathrm{PCC}}(t)$. The peak value of the PCC voltage is shown in Fig. 4 in per unit for different grid conditions over the X/R-ratio at nominal power and unity power factor. The data used for the calculation are shown in Table I. The harmonic current injection level $r_{i,3}$ is set to 4 % as the maximum injection level allowed by grid standards. The solid lines depict the cases without CWFS and the dashed lines show the cases with CWFS. It can be seen that in weak grid conditions the effect on the PCC voltage is higher than in strong grid conditions. Furthermore, it can be followed that the peak reduction remains similar over the X/R-ratio.

The 3rd harmonic apparent power S_3 that is needed for the 3rd harmonic current injection depending on SCR and X/R-ratio is shown in Fig. 5 in per unit under the assumption of unity power factor at fundamental frequency. The power level

TABLE I
DATA FOR ANALYSIS

$V_{\mathrm{g}} = V_{\mathrm{base}}$	400 V
$V_{1,\mathrm{g}}$	230 V
ω_0	$2\pi 50\,\mathrm{s}^{-1}$
$S_{\mathrm{N,PV}} = S_{\mathrm{base}}$	10 kVA
$X_{Lf} (= \omega_0 L_{\mathrm{f}})$	0.08 pu
$r_{i,3}$	0.04

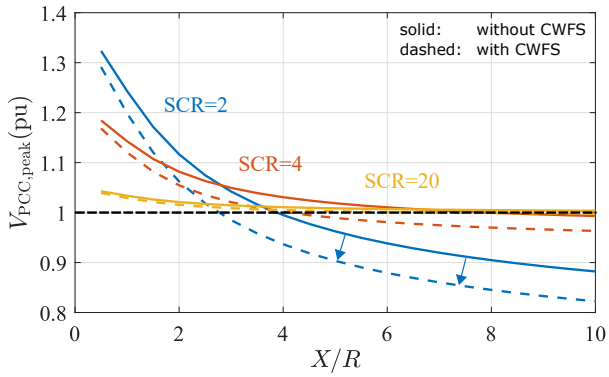

Fig. 4. Voltage level at PCC in relationship to SCR and X/R-ratio at nominal power ($\cos\varphi_{1,\mathrm{x}}=1$).

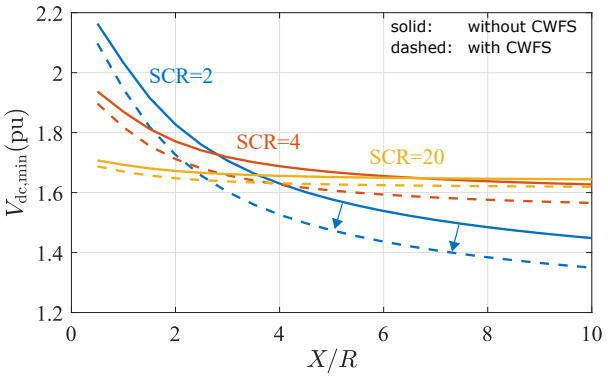

Fig. 6. Minimum dc-link voltage level in relationship to SCR and X/R-ratio at nominal power ($\cos\varphi_{1,\mathrm{x}}=1$).

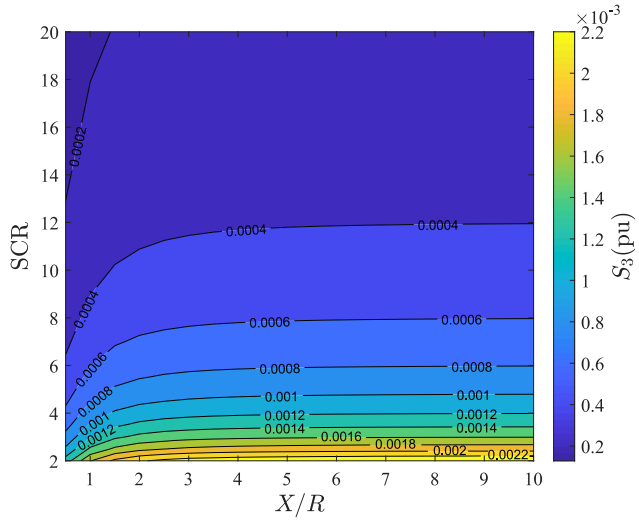

Fig. 5. Power level of the needed injection of 3rd harmonic in relationship to SCR and X/R-ratio at nominal power ($\cos\varphi_{1,\mathrm{x}}=1$).

is higher in weak grid conditions, but the harmonic power level remains low in all conditions at nominal power operation. This indicates that the proposed approach is not leading to increased inverter power ratings and S_3 can be neglected in the analysis:

$$P = P_{1,\mathrm{PCC}}\,. \tag{14}$$

The inverter current rating is not changing, as the rms is only marginally increased by an additional 4 % current component. Fig. 5 illustrates the grid conditions, in which the 3rd harmonic current injection is most effective. Since the amplitude of the injected harmonic current is fixed, the apparent power is equivalent to the respective PCC voltage component. Weak grids with low SCR offer the highest potential over a wide X/R-ratio, only in resistive grids the effect is lower.

D. Influence on Inverter DC-Link Voltage Level

Generally, the injection of harmonic currents lead to additional voltage components across passive elements such as grid filter and cabling. This requires a minimum dc-link voltage level that enables the inverter to provide sufficiently high voltages. A three-phase, four-wire inverter needs to be able to block the phase-to-neutral voltages with half of its dc-link voltage. If the LCL-filter is approximated as an L-filter with inductance L_f and negligible resistance R_f and if the cable impedance is neglected due to short distance between inverter and filter, the minimum dc-link voltage can be calculated:

$$\begin{aligned} V_{\mathrm{dc,min}} &= 2\cdot\max\Big\{\Big|v_{\mathrm{PCC}}+v_{Lf}\Big|\Big\} \\ &= 2\cdot\max\Big\{\Big|\hat{V}_{1,\mathrm{g}}\sin(\omega_0 t) \\ &\qquad +R_\mathrm{g}\sum_{m=1}^{3}\hat{I}_{m,\mathrm{PCC}}\cdot\sin(m\omega_0 t+\varphi_{m,\mathrm{PCC}}) \\ &\quad +\omega_0(L_\mathrm{g}+L_\mathrm{f})\sum_{m=1}^{3}m\hat{I}_{m,\mathrm{PCC}}\cdot\cos(m\omega_0 t+\varphi_{m,\mathrm{PCC}})\Big|\Big\} \end{aligned} \tag{15}$$

where $\hat{V}_{1,\mathrm{g}}$ is the grid voltage amplitude at fundamental frequency and $\hat{I}_{m,\mathrm{PCC}}$ is the PCC current amplitude at the mth harmonic frequency. From the filter approximation it follows that PCC and inverter currents are equal:

$$\underline{I}_{\mathrm{inv}} = \underline{I}_{\mathrm{PCC}}\,. \tag{16}$$

The minimum dc-link voltage depending on X/R-ratio and SCR for nominal power injection is depicted in Fig. 6, where the filter reactance X_{Lf} is assumed. The curves are similar to Fig. 4 with the difference that the effect of CWFS on the minimum dc-link voltage is qualitatively higher than on the PCC voltage level in strong grid conditions. The variation of the minimum dc-link voltage level

$$\Delta V_{\mathrm{dc,min}} = (V^{(2)}_{\mathrm{dc,min}} - V^{(1)}_{\mathrm{dc,min}})/V^{(1)}_{\mathrm{dc,min}} \tag{17}$$

depending on X/R-ratio and power level is shown in Fig. 7 in detail for three different SCR conditions. An overview of the grid conditions used in Fig. 7 is illustrated in Table II. As already concluded above, the effect of CWFS is higher in weak grids with mainly inductive grid impedance. Such condition is depicted in Fig. 7(a). While the variation reaches –6.9 % in mainly inductive grids, the variation reduces to –2.1 % in mainly resistive grids. In strong grids, the variation decreases as it is shown in Fig. 7(e). Here, the minimum dc-link voltage

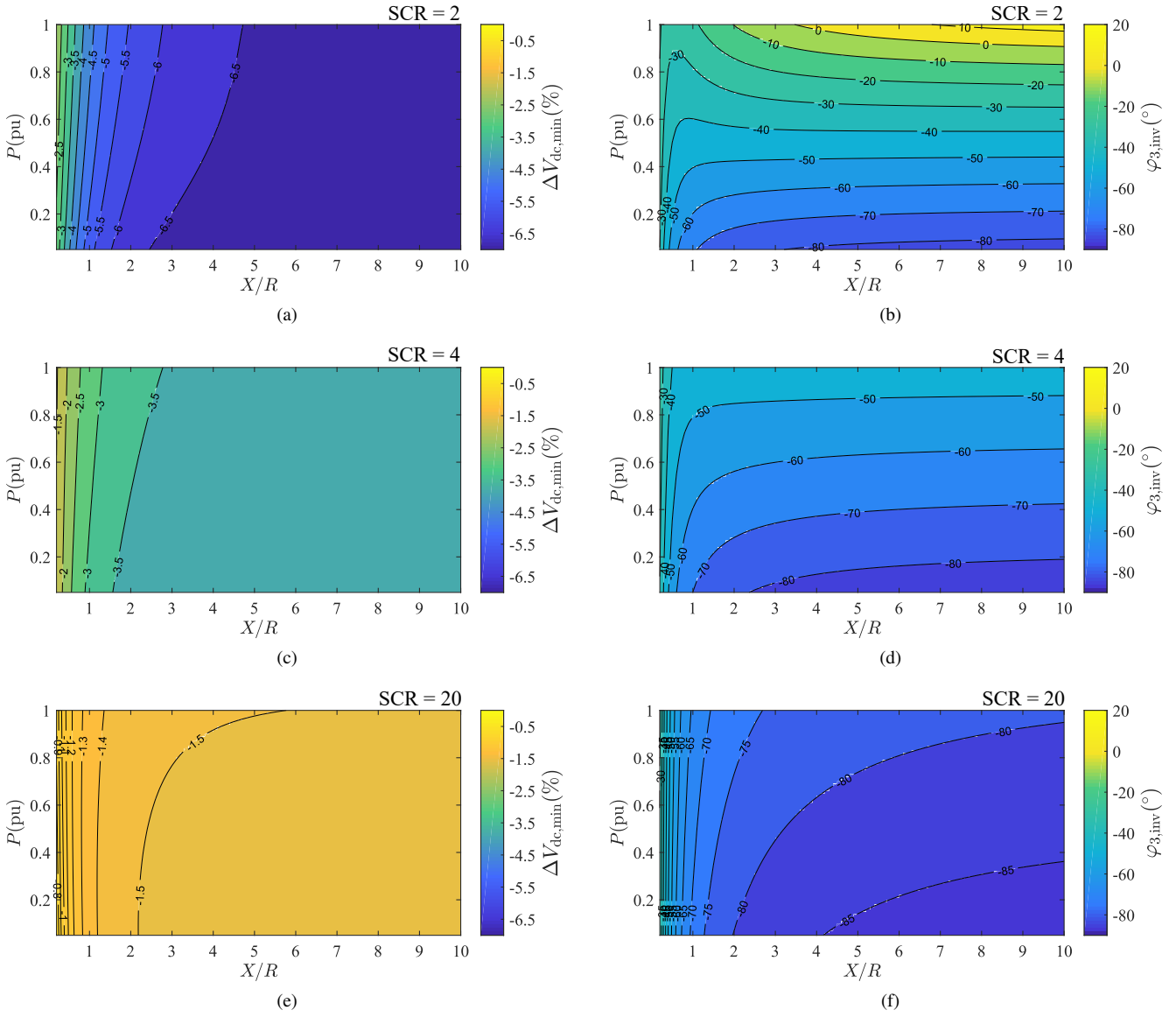

Fig. 7. Effect of CWFS in different grid conditions at unity fundamental power factor ($\cos\varphi_{1,x}=1$): (a) $\Delta V_{\mathrm{dc,min}}$ in weak grids (SCR$=$2), (b) calculated $\varphi_{3,\mathrm{inv}}$ in weak grids (SCR$=$2), (c) $\Delta V_{\mathrm{dc,min}}$ in weak grids (SCR$=$4), (d) calculated $\varphi_{3,\mathrm{inv}}$ in weak grids (SCR$=$4), (e) $\Delta V_{\mathrm{dc,min}}$ in strong grids (SCR$=$20), (f) calculated $\varphi_{3,\mathrm{inv}}$ in strong grids (SCR$=$20).

is reduced by up to −1.6 % in mainly inductive grids, which decreases to −0.7 % in mainly resistive grids.

Similarly, the influence of the power level depends on the SCR. The variation of the minimum dc-link voltage level is generally higher in light power conditions, which is due to the increasing voltage component caused by the fundamental current injection. This voltage component is higher in mainly resistive grids than in mainly inductive grids. As a result, the variation in Fig. 7(a) goes down from −6.9 % (light power) to −6.8 % (full power) in mainly inductive grids and from −2.7 % (light power) to −2.1 % (full power) in mainly resistive grids. Fig. 7(a) shows a variation that changes from −1.6 % (light power) to −1.5 % (full power) in mainly inductive grids and from −0.8 % (light power) to −0.7 % (full power) in mainly resistive grids. From the results it can be followed that the proposed approach offers a decreased minimum dc-link voltage level in all grid and power injection conditions. However, the effect is higher at light power injection, optimally in mainly inductive grid conditions.

The respective harmonic phase $\varphi_{3,\mathrm{inv}}$ of the inverter current, which is required to achieve the intended effect on the minimum dc-link voltage as shown in Fig. 7(a),(c),(e), is depicted in Fig. 7(b),(d),(f) for the same grid conditions. While the harmonic phase remains in strong grids relatively close to −90° over a wide range of X/R-ratio and active power level, it deviates more from this value in weak grids. Moreover, the influence of the power level increases so that the harmonic phase becomes positive in Fig. 7(b) at full power, for instance. Fig. 7(b),(d),(f) show that an optimal minimum dc-link voltage reduction can be realized, if the harmonic phase reference calculation takes into account the power level of the PV system and the actual grid condition, for which several on-line grid

TABLE II
CONDITIONS OF RESULTS IN FIG. 7

	SCR	$\Delta V_{\mathrm{dc,min}}$	$\varphi_{3,\mathrm{inv}}$
	2	(a)	(b)
$\cos\varphi_{1,x}=1$	4	(c)	(d)
	20	(e)	(f)

estimation methods can be implemented [17]–[19]. As the previous analysis shows that for strong grids optimal harmonic phase is close to −90°, a straightforward implementation of CWFS that does not require an impedance estimation could assume a fixed phase.

E. Fixed Harmonic Phase

The impact of a fixed harmonic phase on the minimum dc-link voltage variation is shown in Fig. 8 based on the analysis of Fig. 7 and a harmonic phase of −90°. The results show that in this case the minimum dc-link voltage reduction is lower in all grid conditions, which depends on the error between fixed and calculated harmonic phase shown in Fig. 7(b),(d),(f). While the error is small in strong grid conditions, it is more significant in weak grids, increasing with the power level. Fig. 8(a) shows an area around the power level 0.6–0.7 pu in which CWFS offers only a small advantage over operation without CWFS. Above this area, CWFS leads to an increased minimum dc-link voltage. Hence, a fixed harmonic phase results in a less effective approach and a smaller grid operation range that depends on the power level.

F. Impact on PV Output Energy

The influence of a lower minimum dc-link voltage level on the PV output energy depends on the irradiance profile and temperature of the location, the characteristics of the PV module and the number of series modules. In order to estimate the impact of CWFS on the PV output energy, the PV data of a *BP365 65 W* solar module included in *PLECS* software as benchmark is used. The interpolated average daily irradiance of a location in South Denmark in January and July [20] is shown in Fig. 9(a). Assuming equal irradiance conditions among the series modules and a constant temperature of 25 °C, the maximum power point (MPP) of the PV module is calculated in 5 min steps based on the irradiance profile and a chosen number of series modules. The MPP is used, if the MPP voltage of all series PV modules is greater than the minimum dc-link voltage that is chosen in respect to Fig. 2(b). Otherwise, the PV output power is curtailed and set to the power that can be achieved with the minimum dc-link voltage. The resulting PV output energy E is shown in Fig. 9(b),(d),(f) comparing inverter operation without and with CWFS for the different grid conditions at unity X/R-ratio and minimum dc-link voltage values as calculated in Fig. 7. The respective variation of the PV output energy between operation without and with CWFS is depicted in Fig. 9(c),(e),(g) and it can be followed that the effectiveness of CWFS also depends on the level of irradiance, the PV module characteristics and the number of series modules. CWFS can be considered in the design of a PV system with single-stage inverter as a additional degree of freedom to increase the energy output.

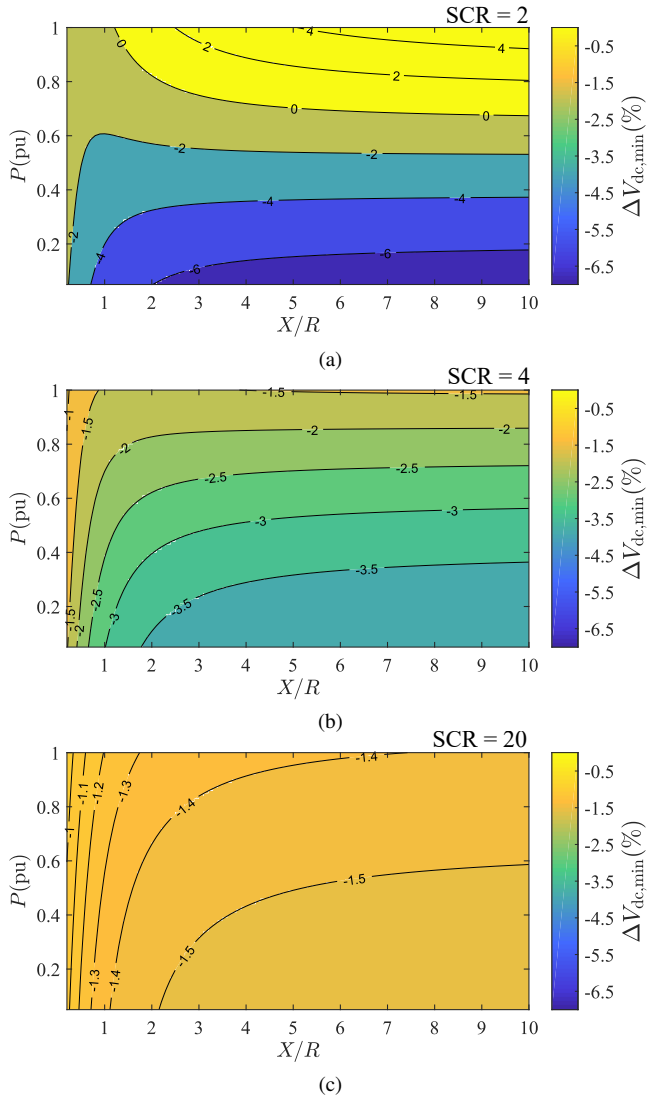

Fig. 8. Effect of CWFS on variation of the minimum dc-link voltage for different SCR at fixed harmonic phase ($\varphi_{3,\mathrm{inv}} = -90°$,$\cos\varphi_{1,x} = 1$): (a) Weak grid (SCR = 2), (b) weak grid (SCR = 4), (c) strong grid (SCR = 20).

G. Influence on RMS Current Level

It is concluded from Fig. 5 that the proposed 3rd harmonic current injection is not reducing the available power for the fundamental component and the inverter power rating is not increased. The behavior of the rms current in per unit depending on the power injection and SCR is shown in Fig. 10(a) for mainly resistive grids. Even though CWFS is not significantly changing the current level, it can be seen that the difference between current level without and with CWFS becomes larger in light power conditions. ΔI_{PCC} is depicted in Fig. 10(b) depending on X/R-ratio and power level for a weak grid. Similar results are obtained in all grid conditions due to the fixed harmonic current level. Though the current level in light power conditions is increased by 20–30 %, the efficiency of the proposed approach depends on the PV system efficiency,

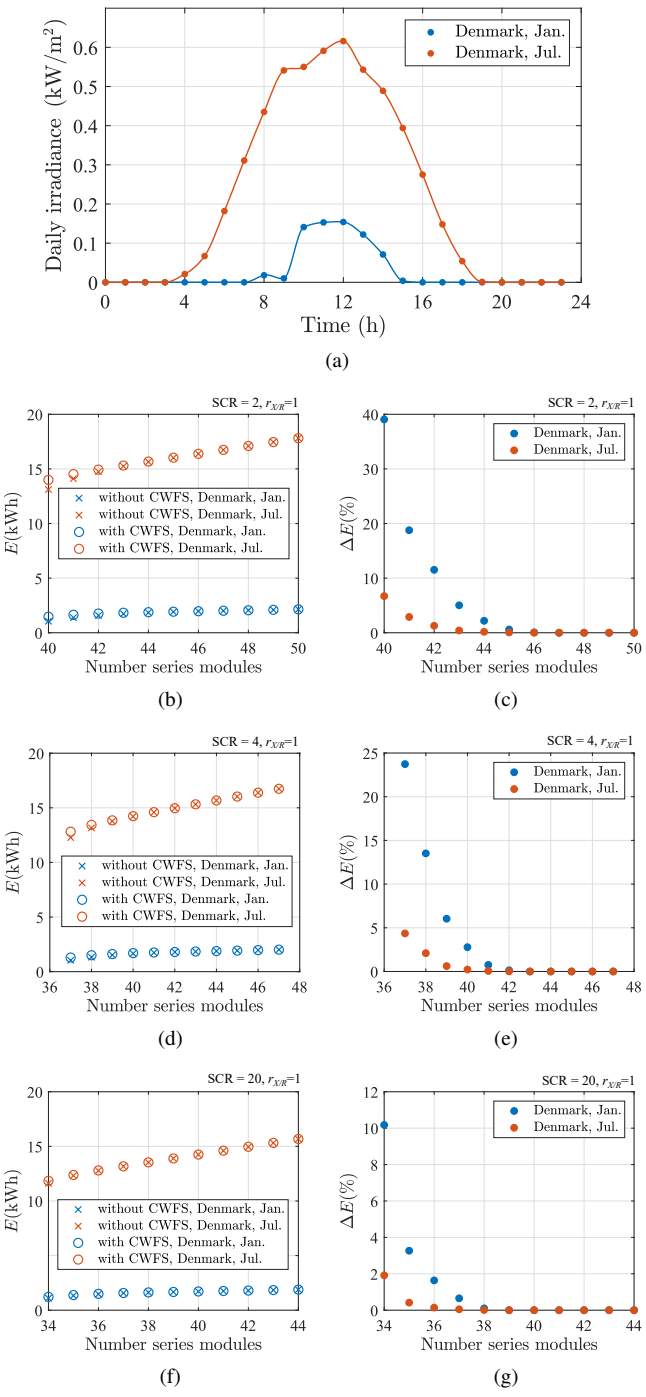

Fig. 9. Influence of CWFS on PV output energy of series *BP365 65 W* solar modules: (a) Average daily irradiance in South Denmark (fixed PV plane with 35° slope and 0° azimuth), (b) PV output energy in weak grid (SCR = 2), (c) variation of PV output energy in weak grid (SCR = 2), (d) PV output energy in weak grid (SCR = 4), (e) variation of PV output energy in weak grid (SCR = 4), (f) PV output energy in strong grid (SCR = 20), (g) variation of PV output energy in strong grid (SCR = 20).

grid parameters and increased PV system utilization rate that is achieved by the extended operation range.

H. Discussion of Harmonic Injection Level

A main constraint of the proposed approach is to stay in compliance with the grid standards such as [15]. A higher

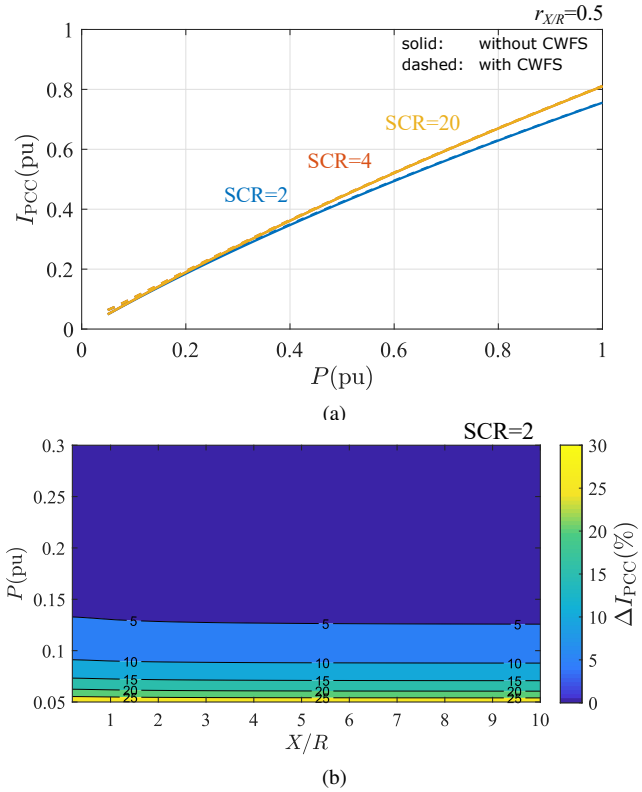

Fig. 10. Effect of CWFS on inverter current level ($\cos\varphi_{1,x} = 1$): (a) Current level without and with CWFS for different SCR, (b) variation of inverter current in weak grid condition.

harmonic injection level might offer a higher potential to lower the PCC voltage level, but it would require to discuss and analyze its impact on the grid and, more importantly, to change grid standards. In the context of an increasing amount of power electronics interfaced grid components, which offer a better susceptibility to harmonics than conventional grid components, adapting the grid standards is a point of discussion [21]. However, the focus of this work is the implementation in frame of the actual grid situation, where grid component operation is not affected, if the limits of grid standards are not violated. PV power plants are usually connected to delta-star transformers, which block the 3rd harmonic frequency from flowing into the medium voltage grid. The loss calculation of distribution transformers in presence of non-sinusoidal currents is described in [22], providing a calculation example based on a standard IEEE 225 kVA transformer with rated full load current of 624.5 A. Even though the current has a high harmonic content I_m/I at the 1st harmonic (97 %), 3rd harmonic (37 %), 5th harmonic (35 %) and 7th harmonic (10 %), the transformer current capability is only reduced to 75.4 % of its rated value. This shows that a harmonic injection level of 4 %, used in the proposed approach, is not affecting the current capability of distribution transformers.

III. Implementation of Current Waveform Shaping

Implementing CWFS requires minor extensions of standard grid inverter control structures to account for the harmonic reference calculation and control. A basic CWFS control

concept is presented, which is extended by a grid impedance estimation algorithm for optimal harmonic phase operation. Simulation results validate the analysis of minimum dc-link voltage variation by 3rd harmonic current injection.

A. Inverter Control of Current Waveform Shaping

The CWFS control concept for grid-connected PWM inverters to inject 3rd harmonic current in addition to the fundamental current component is explained using the example of a single-phase inverter system shown in Fig. 11(a) that is based on an open-loop PQ control. The control can be easily adapted for three-phase, four-wire systems as these systems can be seen as combination of three single-phase systems in the simplest implementation. PV inverters are usually connected to the grid by an LC- or LCL-filter. The cascaded control structure of Fig. 11(a) is valid in both cases, but the LC-filter is chosen due to the simpler representation. If an LCL-filter is adopted, the grid-side filter inductance is part of the grid impedance. The current controller is based on proportional resonant (PR) control for 50 Hz current reference tracking and it features a harmonic compensator (HC) to track the 3rd harmonic reference. Either the current i_{PCC} or the inverter current i_{inv} is controlled both leading to an error, as the calculation of φ_3^* is based on the grid filter approximation ($\varphi_{3,\mathrm{inv}}$ and $\varphi_{3,\mathrm{PCC}}$ are equal). The difference between i_{inv} and i_{PCC} in the real system depends on the parameters and is usually small, since the grid filter is designed to filter high-order harmonics, but it can be compensated if required.

A detailed view of the fundamental current reference block is depicted in Fig. 11(b), where the active and reactive power references and the quadrature signal components v_α and v_β of the grid filter capacitor voltage are the inputs. The harmonic reference block is shown in Fig. 11(c) with the nominal current amplitude $\hat{I}_{\mathrm{N,PCC}}$, the voltage angle θ_1 and the reference of the harmonic current phase φ_3^* as inputs. In order to determine the 3rd harmonic amplitude, $\hat{I}_{\mathrm{N,PCC}}$ is multiplied by the harmonic current injection level $r_{i,3}$. The harmonic phase can be fixed or it is calculated by on-line grid estimation algorithms as noted above. The output i_{inv}^* is finally obtained by adding both sinusoidal waveforms.

The active power reference P^* is generated from the dc power P_{dc} supplied by the PV array. Standard single-phase second-order generalized integrator (SOGI) based PLL [23] or frequency-locked loops (FLL) are possible solutions for grid synchronization as these methods provide the quadrature signal components of the PCC voltage, which are needed for fundamental reference calculation.

B. Harmonic Phase Determination Based on Grid Impedance Estimation

For an optimal harmonic current injection, the harmonic phase can be determined based on the analysis of Fig. 7(b),(d),(f). Instead of using a fixed harmonic phase in Fig. 11(a), a look-up table provides the angle depending on the power reference P^* and the X/R-ratio of the grid impedance. As noted above, the X/R-ratio can be estimated on-line by different solutions, which can be classified in

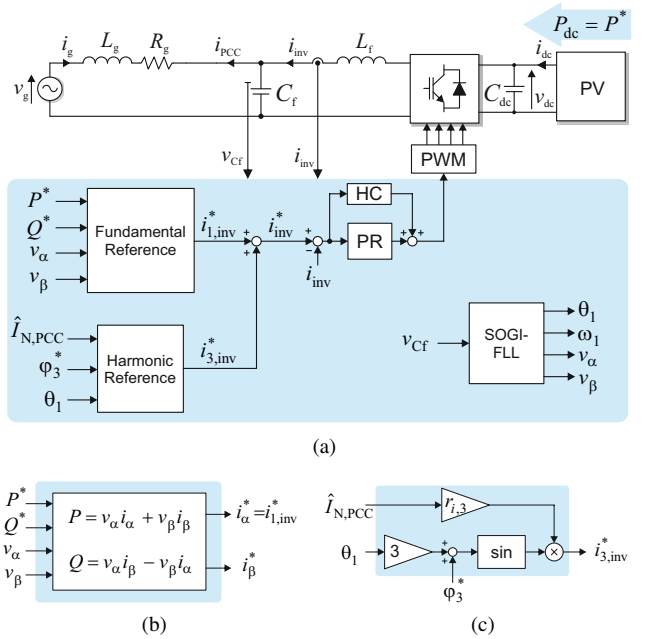

Fig. 11. CWFS control concept of single-phase PV inverter with LC-filter: (a) PQ open loop control structure, (b) fundamental current reference calculation, (c) harmonic current reference calculation.

non-invasive (passive) methods, invasive (active) methods and quasi-invasive methods [19]. Due to its simple calculation algorithm and the usage of the same control principle (SOGI based), the active and reactive power variation approach [17], [24] is chosen for extending Fig. 11(a) by harmonic phase determination. The harmonic phase determination is shown in Fig. 12(a) and the algorithm of active and reactive power variation is depicted in Fig. 12(b), which is described in [24]. The response of i_{inv} and v_{Cf} to power variations is measured and the grid resistance and inductance can be calculated based on the different grid operation points. While the grid resistance follows from active power variation, the grid inductance is calculated based on reactive power variation. The quadrature signal component of the grid current generated by a SOGI is needed for dq-transformation, since the impedance calculation is in synchronous reference frame. The dq-components of PCC current and grid filter capacitor voltage are filtered by a notch filter [17] before used for impedance calculation.

C. Steady-State Simulation Results

The proposed CWFS control approach of Fig. 11 and the harmonic phase determination based on impedance estimation of Fig. 12 are validated by simulation using *MATLAB Simulink* and *PLECS Blockset*. The simulation data of a 3.7 kVA PV inverter are given in Table III, assuming a constant dc-link voltage level. The filter inductance L_{f} of the passively damped LC-filter is chosen based on X_{Lf} in Table I for a SCR of 20 and a X/R-ratio of 1 in order to validate the analysis results. The power variation ΔP and ΔQ of the grid estimation algorithm are set to 0.05 pu. The minimum dc-link voltage variation in steady-state is shown in Fig. 13(a) for active power operation from 0.1 pu to 1 pu. Both CWFS with fixed harmonic phase of $-90°$ and CWFS with harmonic phase

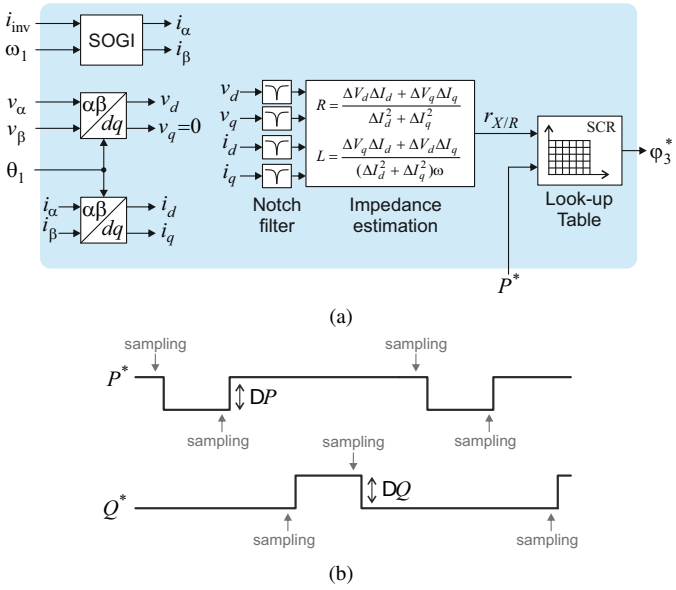

Fig. 12. Harmonic phase determination based on look-up table and grid impedance estimation by PQ-variation: (a) Control structure, (b) active and reactive power variation.

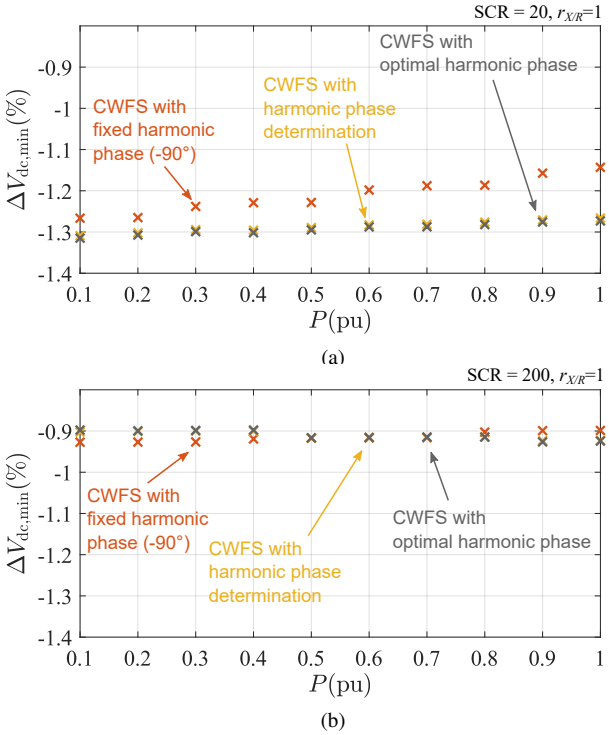

Fig. 13. Minimum dc-link voltage variation of a single-phase PV inverter and unity X/R-ratio in steady-state: (a) strong grid (SCR = 20), (b) increased SCC of connection point by factor 10 (SCR = 200).

determination are in accordance with the analysis in Fig. 7(e) and Fig. 8(c), respectively. Furthermore, it is shown that the grid impedance estimation leads to the same results as if the theoretical harmonic phase (shown in gray) is directly applied. The same inverter configuration is tested at a connection point with a 10 times larger SCC, which results in an SCR of 200. This represents a case of a 3.7 kVA PV system at a connection point of a LV feeder with an SCC of 740 kVA. The obtained minimum dc-link voltage variation is depicted in Fig. 13(b) showing that CWFS with constant harmonic phase and CWFS with grid impedance estimation lead to similar results around 0.9 % voltage reduction. Hence, a harmonic phase determination approach is not required in such condition for optimizing the effect on the minimum dc-link voltage.

D. Simulation Results of Dynamic Behavior at Output Power Variation

The error of the current controller during a power step of 0.1 pu is shown in Fig. 14 based on the simulation data given in Table III including the control parameters, where k_p is the proportional gain of the current controller and $k_{\mathrm{res},m}$ the gain of the resonant part at the mth order harmonic frequency.It is important to note that this is not an optimal set of control parameters. The power step is initiated after 0.1 s jumping from an output power at fundamental frequency of 0.1 pu to 0.2 pu. The behavior at normal operation without CWFS is depicted in Fig. 14(a) and the behavior with active CWFS is shown in Fig. 14(b). In both cases, the simulation includes different grid conditions and it can be concluded that CWFS is not significantly changing the dynamic behavior of the inverter operation. For implementation in real applications, the control parameters must be tuned compromising fast response, low steady-state error and disturbance rejection in respect of the grid conditions and the inverter parameters.

IV. Experimental Results

The effectiveness of the proposed approach is shown by experiments. The setup consists of a 7.1 kW *Danfoss FC302* three-phase inverter shown in Fig. 15(a) with passively damped LC-filter and customized control interface. The inverter is operated in single-phase configuration by a *dSPACE 1006* based on Fig. 11 controlling the inverter current. The dc side of the inverter is connected to a 10 kW dc power supply and the open-loop PQ-control of Fig. 11(a) is inactive by which the ac current reference can be directly set. The ac side of the inverter is connected through a standard single-phase isolation transformer and 100 m cable to the *Spitzenberger PAS1500*, shown in Fig. 15(b), which provides a sinusoidal grid voltage. The isolation transformer is needed to avoid ground loops between the dc power supply and the *Spitzenberger PAS1500*.

TABLE III
Simulation Data

V_g	230 V
L_f	3.4 mH
C_f	5 µF
$R_{\mathrm{f,damp}}$	4 Ω
f_S	10 kHz
V_dc	400 V
$S_{\mathrm{N,PV}}$	3.7 kVA
$r_{i,3}$	0.04
k_p	20
$k_{\mathrm{res},1}$	1000
$k_{\mathrm{res},3}$	1000

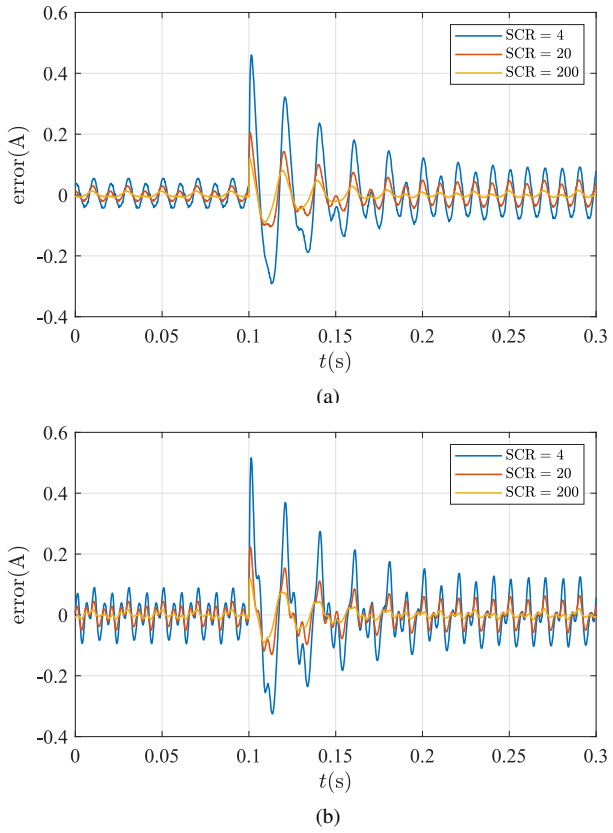

Fig. 14. Current control error during an output power step of 0.1 pu: (a) Normal operation without CWFS, (b) operation with CWFS.

Its inductance L_t constitutes an LCL-filter in combination with the LC-filter of the inverter. The setup data are given in Table IV and an overview is depicted in Fig. 15(b). The capacitor voltage v_Cf and the PCC current i_PCC are measured. Based on the grid data and the nominal inverter current $I_\mathrm{N,inv}$, the SCR is calculated showing a strong grid condition with resistive grid characteristic due to the LV cable connection. The experimental tests include the steady-state evaluation of inverter operation at the described grid condition and at a grid condition with an additional grid inductance. Furthermore, tests are conducted to illustrate the extended dc-link voltage operation range and to show the dynamic behavior of a possible transition mechanism between operation with and without CWFS.

A. Steady-State CWFS Measurement Results

The inverter operation is tested for low and medium active power injection at fundamental frequency. With activated CWFS, a 3rd harmonic current with an amplitude of 4 % of the rated inverter current is added to the reference. The phase φ_3^* is changed manually in order to achieve the highest effect on the peak voltage level, for which the harmonic phase determination of Fig. 12 can be implemented in real applications. In the experimental tests, a fixed harmonic phase of −90° is used for harmonic current injection. The grid filter capacitor voltage and PCC current waveforms are shown in Fig. 16 for a fundamental current amplitude of 2 A in both cases without (fundamental) and with activated CWFS. A zoomed view on the peak value of v_Cf, in which the high frequency components are filtered, is shown in Fig. 16(a). It can be concluded that the voltage peak value is reduced by

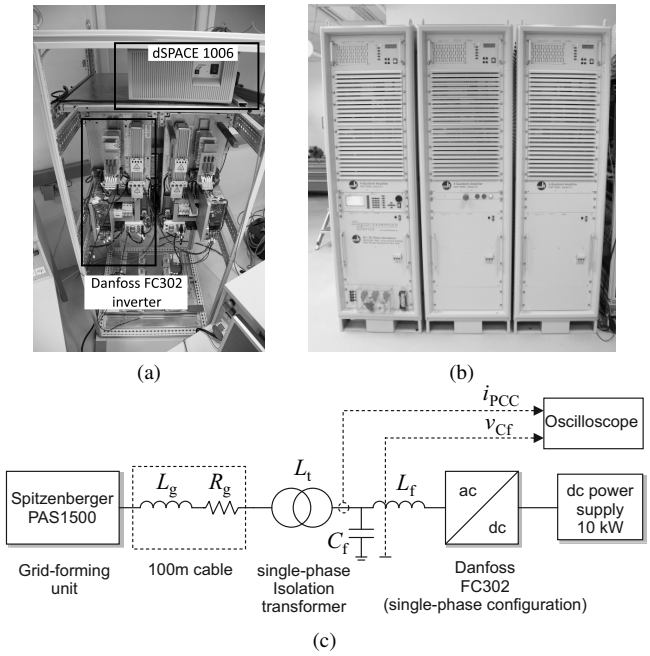

Fig. 15. Experimental setup: (a) Danfoss inverter system (FC302) in single-phase configuration, (b) Spitzenberger PAS1500, (c) setup overview.

TABLE IV
SETUP DATA

Grid data	$V_\mathrm{N,PCC}$	230 V
	L_g	955 µH
	R_g	800 mΩ
	L_t	500 µH
	SCR	34
	$r_{X/R}$	0.571
Inverter data	L_f	5.2 mH
	C_f	5 µF
	$R_\mathrm{f,damp}$	4 Ω
	V_dc	400 V
	f_S	10 kHz
	$I_\mathrm{N,inv}$	7 A
	$r_{i,3}$	0.04

TABLE V
SUMMARY OF MEASUREMENT RESULTS (SCR = 34, $r_{X/R} = 0.571$)

$\frac{\hat{I}^*_\mathrm{1,inv}}{\sqrt{2}}$		Δv_Cf	$\frac{\Delta v_\mathrm{Cf}}{V^{(1)}_\mathrm{Cf,peak}}$	THD_v	TDD_i	I_PCC
0.5 A	(1)	-	-	1.67 %	0.21 %	0.49 A
	(2)	−6.12 V	−1.9 %	1.04 %	3.97 %	0.56 A
1.41 A	(1)	-	-	1.85 %	0.43 %	1.41 A
	(2)	−6.66 V	−2.04 %	1.55 %	3.97 %	1.43 A
2.47 A	(1)	-	-	2.12 %	0.82 %	2.44 A
	(2)	−6.19 V	−1.88 %	1.48 %	4.02 %	2.46 A

(1) Case without CWFS, (2) Case with CWFS

TABLE VI
SUMMARY OF MEASUREMENT RESULTS WITH ADDITIONAL GRID INDUCTANCE (SCR = 18.5, $r_{X/R} = 1.985$)

$\frac{\hat{I}^*_{1,\mathrm{inv}}}{\sqrt{2}}$		Δv_{Cf}	$\frac{\Delta v_{\mathrm{Cf}}}{V^{(1)}_{\mathrm{Cf,peak}}}$	THD_v	TDD_i	I_{PCC}
0.5 A	(1)	-	-	1.94 %	0.21 %	0.47 A
	(2)	−8.28 V	−2.56 %	1.14 %	3.87 %	0.54 A
1.41 A	(1)	-	-	2.12 %	0.45 %	1.38 A
	(2)	−8.32 V	−2.56 %	1.42 %	3.96 %	1.41 A
2.47 A	(1)	-	-	2.32 %	0.7 %	2.45 A
	(2)	−7.9 V	−2.42 %	1.61 %	4.05 %	2.46 A

(1) Case without CWFS, (2) Case with CWFS

CWFS. Looking at the absolute peak values of the filtered waveforms in both cases, Δv_{Cf} can be calculated. The results are shown in Table V for three different current references (absolute and relative value). In addition, the 3rd harmonic voltage component in relation to the fundamental voltage component without CWFS, the 3rd harmonic voltage amplitude in relation to the fundamental voltage component are evaluated. Furthermore, the total harmonic distortion (THD) of the PCC voltage waveform and the total demand distortion (TDD) of the current waveform as well as its rms value are calculated. As expected from the analysis in Section II, the peak value of the voltage waveform is reduced in the tested conditions. Due to the high SCR of the tested grid, the effect on the voltage is relatively low, as shown in Fig. 1. The results indicate that the impact on the voltage THD remains small and limitations set by grid standards are not exceeded. The current TDD is close to 4 % as set by the CWFS reference. With increasing current reference, the current TDD increases and exceeds marginally the 4 % level at medium active power injection. This behavior can be avoided by controlling the PCC current, by compensating the grid filter parameters in the control or by reducing the harmonic reference. The calculated rms of the PCC current shows a small variation between operation without and with CWFS at very low current references. Above a current amplitude of 2 A, the difference is negligible and it can be concluded that CWFS is only marginally increasing the losses which can be can be justified with achieving an extended voltage operation range.

The measurements are repeated inserting an additional grid inductance of 3.6 mH, by which the grid becomes weaker and less resistive. The results are summarized in Table VI showing that the effect on the voltage peak value is higher than in the measurements with higher SCR, which is in accordance with the analysis. The voltage THD stays in compliance with grid standards and the current TDD and rms value reveal the same behavior as in the measurements with higher SCR.

B. Extended DC-Link Voltage Operation Range

The minimum dc-link voltage level is measured for the same test conditions and a step-wise reduction of the dc-link voltage during inverter operation. The identification of operational and non-operational area is realized by a flag inside the inverter control that detects saturation of the control

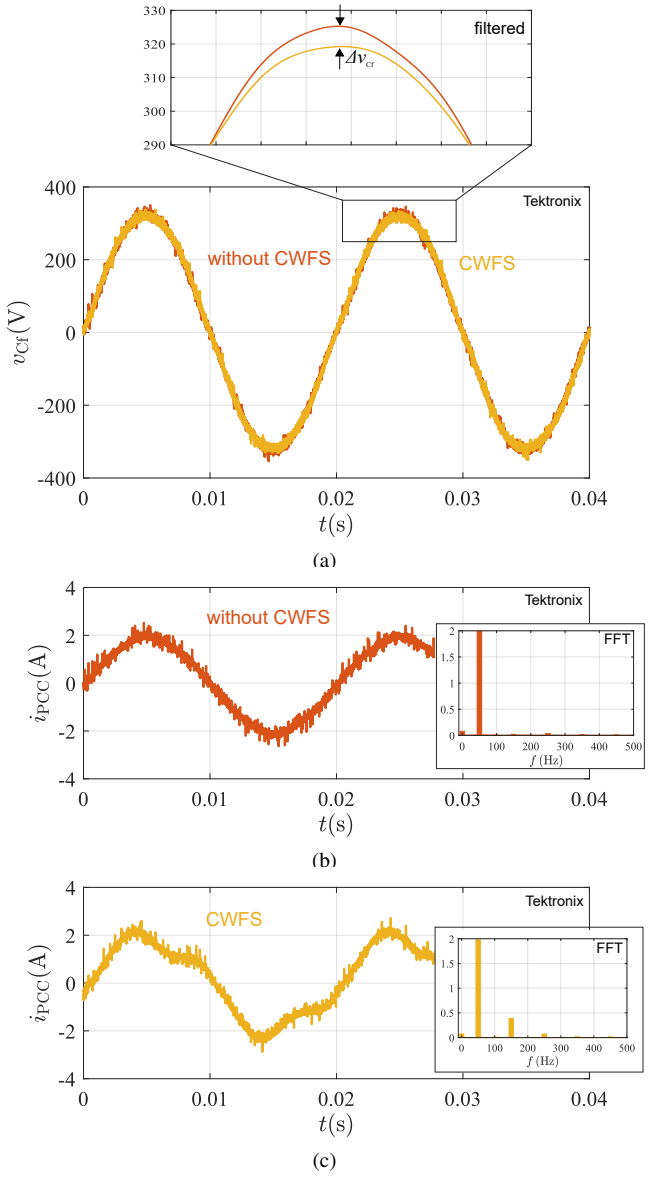

Fig. 16. Grid operation without and with CWFS ($\hat{I}^*_{1,\mathrm{inv}} = 2$ A): (a) Comparison of grid filter capacitor voltage waveforms, (b) PCC current without CWFS, (c) PCC current with CWFS.

output. A resistor parallel to the dc-link guarantees safe operation when the inverter enters the non-operational area. The measured minimum dc-link voltage values without CWFS and with CWFS for the above grid conditions are shown in Table VII. The voltage and current waveforms in case of a 2 A current amplitude reference and grid inductance L_{g} without CWFS is depicted in Fig. 17(a). The control output saturation is detected at 0.04 s, showing a minimum dc-link value of 327 V. However, the PCC current is distorted by harmonics typical for over-modulation even before software detection, which is due to non-optimal calibration of the experimental setup. An FFT of the current waveform after over-modulation detection illustrates the higher order frequency components. The same dc-link voltage value is used in Fig. 17(b) with active CWFS. Control output saturation is not detected and the PCC current is not distorted by harmonic frequencies different to

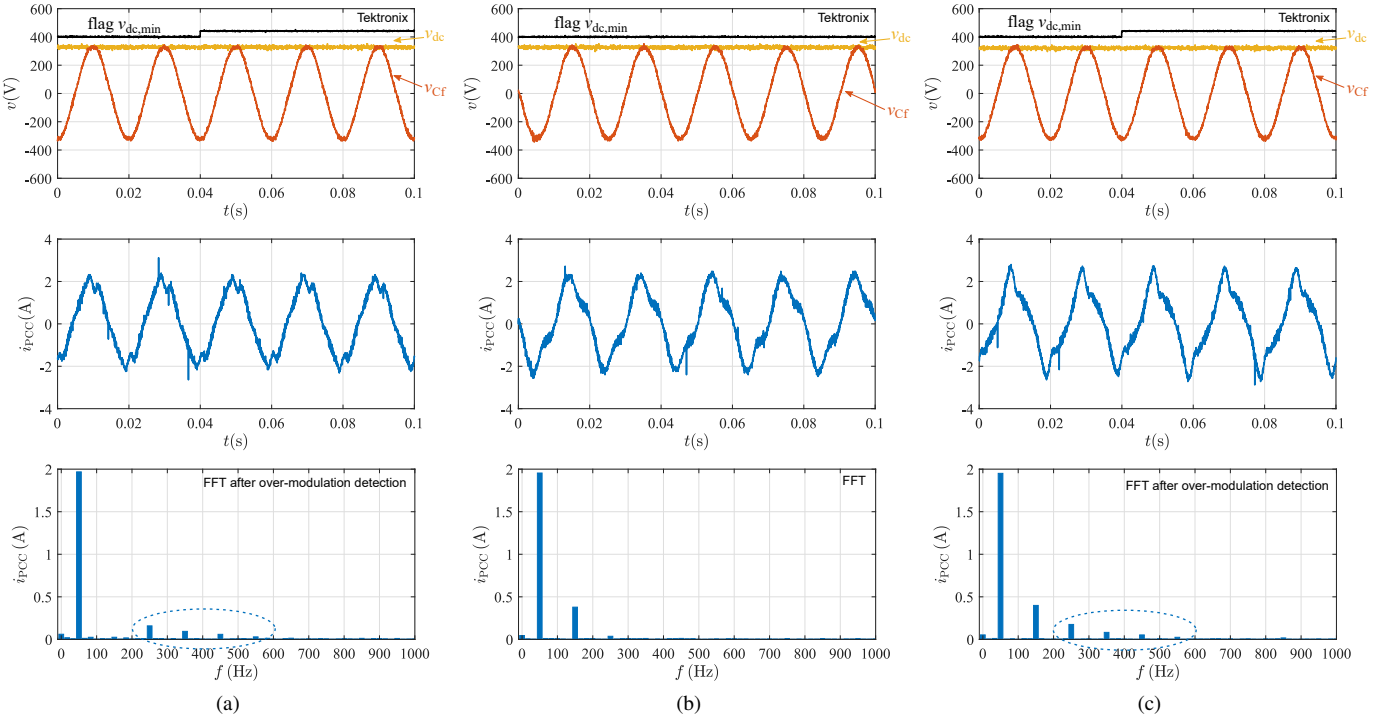

Fig. 17. Measurement of minimum dc-link (2 A current reference): (a) Without CWFS at dc-link voltage of 327 V, (b) with CWFS at dc-link voltage of 327 V, (c) with CWFS at dc-link voltage of 321 V.

TABLE VII
SUMMARY OF MEASURED MINIMUM DC-LINK VOLTAGE REDUCTION

$\hat{I}^*_{1,\mathrm{inv}}$	grid inductance		$V_{\mathrm{dc,min}}$	$\Delta V_{\mathrm{dc,min}}$
0.7 A	L_g	(1)	320 V	-
		(2)	314 V	−1.9 %
	$L_\mathrm{g} + 3.6\,\mathrm{mH}$	(1)	317 V	-
		(2)	310 V	−2.2 %
2 A	L_g	(1)	327 V	-
		(2)	321 V	−1.8 %
	$L_\mathrm{g} + 3.6\,\mathrm{mH}$	(1)	323 V	-
		(2)	316 V	−2.2 %
3.5 A	L_g	(1)	334 V	-
		(2)	327 V	−2.0 %
	$L_\mathrm{g} + 3.6\,\mathrm{mH}$	(1)	331 V	-
		(2)	325 V	−1.8 %

(1) Case without CWFS, (2) Case with CWFS

the 3rd harmonic. If the dc-link voltage is further decreased, the control output saturation is detected at a dc-link voltage of 321 V that is illustrated in Fig. 17(c), leading to a minimum dc-link variation of −1.8 %. The FFT of the PCC current shows higher order frequency components apart from the 3rd harmonic. The results of Table VII are in good agreement with the analysis of CWFS with −90° harmonic phase shift shown in Fig. 8.

C. Transition of CWFS Activation

A possible dc-link voltage protection implementation is depicted in Fig. 18 based on a security voltage level set inside

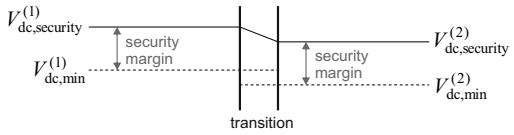

Fig. 18. Protection algorithm of the dc-link voltage security level.

the inverter, which is usually the minimum dc-link voltage level plus a security margin. If the dc-link voltage falls below this level calculated from normal grid operation values, CWFS is activated and the inverter can stay in operation as long as the new minimum dc-link voltage level plus security margin is not violated. For safe operation during the transition, a ramp between both security levels can be used and the security level at CWFS has to be within the security margin of the normal inverter operation. The dc-link voltage v_dc, the grid filter capacitor voltage v_Cf and the PCC current i_PCC during transition between normal inverter operation (without CWFS) and operation with CWFS is shown in Fig. 19. In order to test the protection mechanism without using the real safety margins of the setup, the dc-link voltage is increased to 450 V and the security level of normal operation is set to 420 V. During normal inverter operation, the dc-link voltage is step-wise reduced until it violates the security level and CWFS is activated. The detection instance is highlighted in Fig. 19(a) by the black box. When CWFS is activated, the harmonic reference, implemented with a first order delay and a time constant of 500 ms in order to obtain a smooth transition, increases. As a result, the ac voltage is not showing dynamics

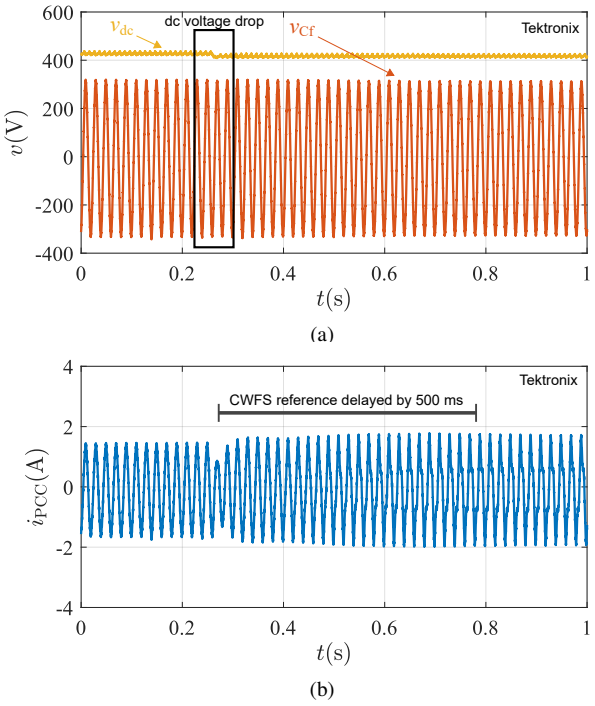

Fig. 19. Transition between operation without and with CWFS: (a) Behavior of grid filter capacitor and dc-link voltages, (b) behavior of PCC current.

such as overshoots, which potentially can lead to violations of the new dc-link voltage security level. The main current dynamics are caused by the reaction of the fundamental frequency current controller to the dc-link voltage drop.

V. Conclusion

This paper has investigated the possibility to extend the operation range of photovoltaic, single-stage voltage source inverters in single-phase and three-phase, four-wire applications by current waveform shaping, decreasing the minimum dc-link voltage level, which leads to an increase of the utilization rate of photovoltaic systems. The extended operation range is achieved without additional components or conversion stages, and leaving the inverter rating unchanged. Standard resonant based control structures and standard synchronization methods can be used for implementation and the optimal harmonic current reference can be calculated by harmonic phase determination based on an on-line grid estimation. Analysis show that the voltage peak value at the point of common coupling is reduced by 3rd harmonic current injection, which is set to the maximum value allowed by grid standards. As a result, lower inverter voltages and consequently a lower dc-link voltage level are required for grid operations. The proposed approach is applicable in a wide grid condition range and grid impedance range, but most effective in light power operation. The analysis shows that up to $-7\,\%$ variation of the minimum dc-link voltage level can be achieved in weak inductive grids. Simulation results validate the analysis and the effectiveness of the proposed control approach. Experimental results verify the effect on the minimum dc-link voltage showing a variation of up to $2.2\,\%$ in strong grid conditions, while complying with the grid standards.

References

[1] M. Ashabani, Y. A.-R. I. Mohamed, M. Mirsalim, and M. Aghashabani, "Multivariable droop control of synchronous current converters in weak grids/microgrids with decoupled *dq*-axes currents," *IEEE Trans. Smart Grid*, vol. 6, no. 4, pp. 1610–1620, 2015.

[2] R. Zhu, G. de Carne, F. Deng, and M. Liserre, "Integration of large photovoltaic and wind system by means of smart transformer," *IEEE Trans. Ind. Electron.*, vol. 64, no. 11, pp. 8928–8938, 2017.

[3] D. Chen, J. Jiang, Y. Qiu, J. Zhang, and F. Huang, "Single-Stage Three-Phase Current-Source Photovoltaic Grid-Connected Inverter High Voltage Transmission Ratio," *IEEE Trans. Power Electron.*, vol. 32, no. 10, pp. 7591–7601, 2017.

[4] S. B. Kjaer, J. K. Pedersen, and F. Blaabjerg, "A review of single-phase grid-connected inverters for photovoltaic modules," *IEEE Trans. Ind. Appl.*, vol. 41, no. 5, pp. 1292–1306, 2005.

[5] T. Esram and P. L. Chapman, "Comparison of photovoltaic array maximum power point tracking techniques," *IEEE Trans. Energy Convers.*, vol. 22, no. 2, pp. 439–449, 2007.

[6] T. Messo, J. Jokipii, J. Puukko, and T. Suntio, "Determining the Value of DC-Link Capacitance to Ensure Stable Operation of a Three-Phase Photovoltaic Inverter," *IEEE Trans. Power Electron.*, vol. 29, no. 2, pp. 665–673, 2014.

[7] W. Xiao, W. Dunford, P. Palmer, and A. Capel, "Regulation of Photovoltaic Voltage," *IEEE Trans. Ind. Electron.*, vol. 54, no. 3, pp. 1365–1374, 2007.

[8] E. Serban, F. Paz, and M. Ordonez, "Improved PV inverter operating range using a miniboost," *IEEE Trans. Power Electron.*, vol. 32, no. 11, pp. 8470–8485, 2017.

[9] Y. Fang and X. Ma, "A novel pv microinverter with coupled inductors and double-boost topology," *IEEE Trans. Power Electron.*, vol. 25, no. 12, pp. 3139–3147, 2010.

[10] X. Hu, P. Ma, B. Gao, and M. Zhang, "An integrated step-up inverter without transformer and leakage current for grid-connected photovoltaic system," *IEEE Trans. Power Electron.*, vol. 34, no. 10, pp. 9814–9827, 2019.

[11] O. Ojo, "The Generalized Discontinuous PWM Scheme for Three-Phase Voltage Source Inverters," *IEEE Trans. Ind. Electron.*, vol. 51, no. 6, pp. 1280–1289, 2004.

[12] S. Brüske, G. Buticchi, and M. Liserre, "Multifrequency single-phase islanded grids," *IEEE Trans. Ind. Electron.*, vol. 65, no. 12, pp. 9528–9538, 2018.

[13] Z. Yuan, S. W. H. d. Haan, J. B. Ferreira, and D. Cvoric, "A FACTS device: Distributed power-flow controller (DPFC)," *IEEE Trans. Power Electron.*, vol. 25, no. 10, pp. 2564–2572, Oct. 2010.

[14] R. Alaei and S. A. Khajehoddin, "The operation of a power transmission line with injected third harmonic voltage," *IEEE Trans. Power Del.*, vol. 32, no. 1, pp. 226–233, Feb. 2017.

[15] *IEEE Recommended Practice and Requirements for Harmonic Control in Electric Power Systems*, IEEE Std. 519-2014, Jun. 2014.

[16] J. Rocabert, A. Luna, F. Blaabjerg, and P. Rodríguez, "Control of power converters in ac microgrids," *IEEE Trans. Power Electron.*, vol. 27, no. 11, pp. 4734–4749, 2012.

[17] M. Ciobotaru, R. Teodorescu, P. Rodriguez, A. Timbus, and F. Blaabjerg, "Online grid impedance estimation for single-phase grid-connected systems using PQ variations," in *IEEE Power Electronics Specialists Conference (PESC 2007)*, 2007, pp. 2306–2312.

[18] M. Liserre, F. Blaabjerg, and R. Teodorescu, "Grid Impedance Estimation via Excitation of LCL-Filter Resonance," *IEEE Trans. Ind. Appl.*, vol. 43, no. 5, pp. 1401–1407, 2007.

[19] N. Hoffmann and F. W. Fuchs, "Minimal Invasive Equivalent Grid Impedance Estimation in Inductive–Resistive Power Networks Using Extended Kalman Filter," *IEEE Trans. Power Electron.*, vol. 29, no. 2, pp. 631–641, 2014.

[20] European Commission. Accessed: Jan. 22, 2020. [Online]. Available: https://re.jrc.ec.europa.eu/pvg_tools/en/tools.html#MR

[21] J. Martynaitis, "Discussion of "Are Harmonic Recommendations According to IEEE and IEC Too Restrictive?"," *IEEE Trans. Power Del.*, vol. 22, no. 2, p. 1263, 2007.

[22] *IEEE Recommended Practice for Establishing Liquid Immersed and Dry-Type Power and Distribution Transformer Capability when Supplying Nonsinusoidal Load Currents*, IEEE Std. C57.110-2018, Rev. C57.110-2008, Jun. 2018.

[23] M. Ciobotaru, R. Teodorescu, and F. Blaabjerg, "A new single-phase PLL structure based on second order generalized integrator," in *37th IEEE Power Electronics Specialists Conf.*, Jun. 2006, pp. 1–6.

[24] A. V. Timbus, P. Rodriguez, R. Teodorescu, and M. Ciobotaru, "Line Impedance Estimation Using Active and Reactive Power Variations," in *IEEE Power Electronics Specialists Conference (PESC 2007)*, 2007, pp. 1273–1279.

Sebastian Brüske (S'14) received the BSc and MSc degree in Electrical Engineering, Information Technology and Business Management from Kiel University, Germany, in 2011 and 2013, respectively. Since 2014 he has been working towards the doctoral degree in Electrical Engineering at the Chair of Power Electronics of Kiel University, Germany. His research interests include power electronics for renewable energy systems and power electronics based distribution.

Giovanni De Carne (S'14-M'17) received the B.Sc. and M.Sc. in Electrical Engineering from Polytechnic University of Bari, Bari (Italy) in 2011 and 2013, respectively. From 2013 to 2018, he carried out his Ph.D. studies at the Chair of Power Electronics at Kiel University, Germany. He defended his doctoral thesis in 2018 on Smart Transformer services for distribution grids, and continued working at Kiel University as post-doc on HVDC control and services until 2019. He is currently the Head of the "Real Time System Integration" group at the Institute for Technical Physics at the Karlsruhe Institute of Technology, working on real time simulations and large-scale power hardware in loop systems. He is Associate Editor of IEEE "Industrial Electronics Magazine" and Springer Journal "Electrical Engineering". He is member of PELS, IES and PES, where is an active author and reviewer of journals and conferences of these societies.

Giampaolo Buticchi (S'10-M'13-SM'17) received the MSc degree in Electronic Engineering in 2009 and the PhD degree in Information Technologies in 2013 from the University of Parma, Italy. In 2012, he was a Visiting Researcher at the University of Nottingham, UK. Between 2014 and 2017 he was a post-doctoral researcher at the Christian-Albrechts-University of Kiel, Germany. He is now Associate Professor in Electrical Engineering at the University of Nottingham Ningbo China, China. His research area is focused on power electronics for renewable energy systems, smart transformer fed micro-grids and dc grids for the More Electric Aircraft. He is author/co-author of more than 140 peer-reviewed scientific papers. He is an Associate Editor of the IEEE Transactions on Industrial Electronics.

Marco Liserre (S'00-M'02-SM'07-F'13) received the MSc and PhD degree in Electrical Engineering from the Bari Polytechnic, respectively in 1998 and 2002. He has been Associate Professor at Bari Polytechnic and from 2012 Professor in reliable power electronics at Aalborg University (Denmark). From 2013 he is Full Professor and he holds the Chair of Power Electronics at Kiel University (Germany). He has published 500 technical papers (1/3 of them in international peer-reviewed journals) and a book. These works have received more than 35000 citations. Marco Liserre is listed in ISI Thomson report "The world's most influential scientific minds" from 2014. He has been awarded with an ERC Consolidator Grant for the project "The Highly Efficient And Reliable smart Transformer (HEART), a new Heart for the Electric Distribution System". He is member of IAS, PELS, PES and IES. He has been serving all these societies in different capacities. He has received the IES 2009 Early Career Award, the IES 2011 Anthony J. Hornfeck Service Award, the 2014 Dr. Bimal Bose Energy Systems Award, the 2011 Industrial Electronics Magazine best paper award and the Third Prize paper award by the Industrial Power Converter Committee at ECCE 2012, 2012, 2017 IEEE PELS Sustainable Energy Systems Technical Achievement Award and the 2018 IEEE-IES Mittelmann Achievement Award.

He Zhang (M'14-SM'18) received his B.Eng. degree in Control Science and Engineering from Zhejiang University, China, in 2002. He obtained the MSc. and Ph.D. degree in electrical machines from The University of Nottingham, UK, in 2004 and 2009 respectively. After this he worked as Research Fellow at the University and Director of BestMotion Technology Centre. He moved to University of Nottingham Ningbo China as Senior Research Fellow in 2014, promoted to Principal Research Fellow in 2016 and to Professor in 2020. Currently he is the Director of Nottingham Electrification Centre (NEC) within the Power electronics, Machines and Control research group in University of Nottingham. His research interests include high performance electric machines and drives for transport electrification.